RSC Advances

PAPER

View Article Online
View Journal | View Issue

Cite this: *RSC Adv.*, 2022, **12**, 22806

Preparation of different morphology Cu/GO nanocomposites and their catalytic performance for thermal decomposition of ammonium perchlorate†

Shengnan Li,[a] Ziteng Niu,[a] Yuke Jiao,[a] Peng Jin,[a] Desheng Yang,[a] Chaofei Bai,[a] Jiaran Liu,[a] Guoping Li *[ab] and Yunjun Luo [ab]

Cu nanoparticles are more active catalytically than CuO nanoparticles, which have been widely studied as catalysts for organic synthesis, electrochemistry, and optics. However, Cu nanoparticles are easily agglomerated and oxidized in air. In this research, columnar, flower-like, bubble-like and teardrop-shaped Cu/GO nanocomposites were fabricated *via* a water-solvent thermal method and high temperature calcination technique using deionized water (H_2O), methanol (CH_3OH), ethanol (CH_3CH_2OH) and ethylene glycol (EG) as the solvent, respectively. The structures, the morphology and the catalytic performance and catalytic mechanism for thermal decomposition of ammonium perchlorate (AP) of the Cu/GO nanocomposites have been studied by X-ray diffraction (XRD), X-ray photoelectron spectroscopy (XPS), transmission electron microscopy (TEM), scanning electron microscopy (SEM), nitrogen adsorption tests (BET), simultaneous thermogravimetry-differential scanning calorimetry (TGA/DSC) and thermogravimetric couplet with Fourier transform infrared spectroscopy (TGA–FTIR), respectively. The experimental results show that the morphology of the Cu/GO nanocomposites has a significant effect on the surface area and the teardrop-shaped Cu/GO nanocomposites have the largest specific surface area and the best catalytic performance among them. When 5 wt% of the Cu/GO nanocomposites was added, the decomposition temperature of AP decreased from 426.3 °C to 345.5 °C and the exothermic heat released from the decomposition of AP increased from 410.4 J g^{-1} to 4159.4 J g^{-1}. In addition, the four morphological Cu/GO nanocomposites exhibited good stability, their catalytic performance for thermal decomposition of AP remained stable after 1 month in air. Excellent catalytic performance and stability were attributed to the strong catalytic activity of pure metal nanoparticles, and GO can accelerate electron movement and inhibit the agglomeration of nanoparticles, as well as the multiple effects of inhibiting the oxidation of Cu nanoparticles in air. Therefore, it has important application potential in high-energy solid propellant.

Received 19th June 2022
Accepted 5th August 2022

DOI: 10.1039/d2ra03772f

rsc.li/rsc-advances

1 Introduction

With the rapid development of aerospace and weaponry technology, propulsion vehicles play a pivotal role.[1,2] For example, launch vehicles that send satellites, space stations, spacecraft, and probes into space, as well as torpedoes and cruise missiles that achieve ultra-long-range precision strikes all require propulsion vehicles to achieve this. As the power source of propulsion vehicle engines, solid propellant is greatly significant. Ammonium perchlorate (AP) is the main component of the composite solid propellant, and its thermal decomposition characteristics directly affect the combustion performance of the propellant.[3,4] However, at present, the decomposition temperature of AP is relatively high, the heat release is relatively low, and the temperature span between the high temperature decomposition peak and the low temperature decomposition peak is too large, resulting in a lack of concentration of the heat release, which is not conducive to the combustion of the propellant. Improving the thermal decomposition performance of AP is of great significance for improving the combustion performance of the propellant.[5–7] The introduction of catalyst can effectively reduce the high temperature decomposition temperature of AP, and lower high temperature decomposition temperature and more heat release can lead to higher combustion rate. Therefore, it is of great significance to develop AP catalyst with excellent performance and change the thermal

[a]*School of Materials Science and Engineering, Beijing Institute of Technology, Beijing, 100081, China*

[b]*Key Laboratory for Ministry of Education of High Energy Density Materials, Beijing Institute of Technology, Beijing, 100081, China*

† Electronic supplementary information (ESI) available See https://doi.org/10.1039/d2ra03772f

decomposition process of AP for further development of propellants.

Transition metal oxide nanoparticles (Fe_2O_3, CuO, TiO_2, Mn_3O_4, and Cr_2O_3) have been shown to be effective catalytic performance for thermal decomposition of AP.[8–13] However, compared with transition metal oxide nanoparticles, transition metal nanoparticles (Ni, Al, *etc.*) are more active in the thermal decomposition of AP than commonly used transition metal oxide nanoparticles.[14–17] Nevertheless, due to their small size, high surface activity, and easy agglomeration, transition metal oxide nanoparticles and transition metal nanoparticles cannot fully contact the medium and reduce the catalytic activity, which is not conducive to the combustion of the propellant, and many excellent properties of nanomaterials are lost.[18,19] Loading them on 2D materials is an effective means to suppress nanoparticle agglomeration.[20–23] Graphene oxide (GO) as a classical 2D material, has many excellent properties, such as large specific surface area, strong mechanical properties (strength of 130 GPa and Young's modulus of 1.0 TPa), good electrical conductivity (carrier mobility of 15 000 cm^2 (V^{-1} s^{-1})), high thermal conductivity (thermal conductivity of 5300 W (m^{-1} K^{-1})) and abundant surface oxygen-containing functional groups.[24] The presence of these oxygen-containing functional groups allows GO to have a large number of active sites, which can attract polar molecules and can be compounded with a variety of nanoparticles to prepare nanocomposites.[25–27] CuO nanoparticles with different morphologies have been prepared, which have good catalytic effect on the thermal decomposition of AP, and the morphology of nanoparticles has a certain influence on the catalytic effect.[28,29] However, the study of the catalytic effect of Cu nanoparticles with higher activity on the thermal decomposition of AP is basically in a blank, so the preparation of Cu nanoparticles with different morphologies is of great significance for the propulsion system.

In this research, four morphologies (columnar, flower-like, bubble-like and teardrop-shaped) Cu/GO nanocomposites were prepared by a water-solvent thermal method using graphene as a carrier under four solvent (H_2O, CH_3OH, CH_3CH_2OH and EG) conditions. Cu nanoparticles was loaded on GO, which effectively hindered the agglomeration of Cu nanoparticles and enhanced the stability of Cu nanoparticles in air. The structures, the morphology and their catalytic performance and catalytic mechanism for thermal decomposition of AP of the Cu/GO nanocomposites have been studied by XRD, XPS, TEM, SEM, BET, TGA/DSC and TGA–FTIR, respectively. It has significant potential for application in high-energy solid propellants.

2 Experimental section

2.1 Materials

Graphene oxide (GO) (>95%, 5–10 μm) was purchased from Suzhou Hengqi Graphene Technology Co. Ltd (China). Nanometer copper oxide (CuO) (99.5% metals basis, 150–250 nm) was purchased from Shanghai Aladdin Biochemical Technology Co., Ltd (China). Deionized water (H_2O) was prepared in laboratory. Copper trihydrate nitrate ($Cu(NO_3)_2 \cdot 3H_2O$), urea, ethanol (CH_3CH_2OH), methanol (CH_3OH) and ethylene glycol (EG) were supplied by Beijing Chemical Reagents Co. (China) and were used as received. Ammonium perchlorate (AP) was purchased from Dalian North Potassium Chlorate Co. Ltd (China) and were dried at 60 °C for 10 h before use.

2.2 Synthesis of Cu/GO nanocomposites

Synthesis of columnar Cu/GO nanocomposites: GO (112.5 mg) and deionized water (15 mL) were added to a 50 mL centrifuge tube, and ultrasonic was performed to uniform dispersion (ultrasonic power 95%, time 60 min) to prepare GO dispersion solution (7.5 mg mL^{-1}). 1.45 g $Cu(NO_3)_2 \cdot 3H_2O$ and 0.961 g urea and 30 mL deionized water were added in a 100 mL centrifuge tube. Then they were stirred manually for 30 min until completely dissolved. 10 mL GO dispersion was added to the fully dissolved solution. The solution was ultrasound for 30 minutes to prepare the precursor solution. Then the precursor solution was transferred to a 100 mL stainless steel autoclave. The synthesis was conducted at 180 °C for 4 h in a oven. The resulting powder was washed three times with ethanol and deionized water. After that, the powder was frozen at −80 °C for 5 hours to obtain the primary product of the nanocomposites. The primary product of the nanocomposites was calcined at 500 °C in a tube furnace (heating rate: 10 °C min^{-1}) for 120 min in Ar. Finally, the columnar Cu/GO nanocomposites be obtained.

Synthesis of flower-like, bubble-like and teardrop-shaped Cu/GO nanocomposites: under the same preparation conditions, different solvents (CH_3OH, CH_3CH_2OH, and EG) were used to obtain flower-like, bubble-like and teardrop-shaped Cu/GO nanocomposites, respectively.

2.3 Preparation of catalytic samples (the Cu/GO-AP mixtures)

A certain amount of AP and Cu/GO nanocomposites were placed into a mortar (the mass ratio of the Cu/GO nanocomposites to AP was 5 : 95), and thoroughly ground until it was uniform, that is, Cu/GO-AP mixtures were obtained.

2.4 Characterization

The structures and the morphology of the Cu/GO nanocomposites were investigated by scanning electron microscope (SEM, ZEISS GeminiSEM 300), transmission electron microscope (TEM, Tecnai G2 F30), high-resolution transmission electron microscopy (HRTEM) and energy-dispersive X-ray spectroscopy (EDS). The X-ray diffraction (XRD) patterns of the samples were measured by Ultima IV X-ray diffraction instrument with Cu Kα source. The elemental composition and oxidation state information of teardrop-shaped Cu/GO nanocomposites and GO were carried out by X-ray photoelectron spectroscopy (XPS, Thermo Scientific K-Alpha). Nitrogen adsorption and desorption isotherms of the Cu/GO nanocomposites were tested by Micromeritics ASAP2460 porosimetry analyzer. Pore size and surface areas were obtained by using the Barrett–Joyner–Halenda (BJH) and Brunauer–Emmett–Teller (BET) method respectively. The catalytic performance was detected by simultaneous thermogravimetry-differential

scanning calorimetry (TGA/DSC1, MettlerToledo) at a heating rate of 10 °C min^{-1} from 30 °C to 500 °C in nitrogen. The catalytic kinetic of the Cu/GO nanocomposites for thermal decomposition of AP was performed on TGA/DSC1 at different heating rate (5 °C min^{-1}, 10 °C min^{-1}, 15 °C min^{-1}, 20 °C min^{-1}) from 30 °C to 500 °C in nitrogen. The catalytic mechanism of the Cu/GO nanocomposites for thermal decomposition of AP was carried out with thermogravimetric couplet with Fourier transform infrared spectroscopy (TGA/DSC3 MettlerToledo, FTIR Nicolet iS50) at a heating rate of 10 °C min^{-1} from 30 °C to 500 °C in nitrogen.

3 Results and discussion

Different morphology Cu/GO nanocomposites were synthesized by a two-step method, as shown in Fig. 1. Firstly, GO was used as the carrier, deionized water (H_2O), methanol (CH_3OH), ethanol (CH_3CH_2OH) and ethylene glycol (EG) were used as solvent respectively and $Cu(NO_3)_2 \cdot 3H_2O$ was used as the precursor. The initial products of $Cu_2(OH)_2CO_3$/GO, Cu_2O/GO, Cu_2O/GO and Cu_2O/GO nanocomposites were respectively synthesized under high temperature and high pressure. The XRD diffraction images of initial products showed in Fig. S1.† Then, the initial product of the nanocomposites was placed in a tubular furnace quartz tube, and calcined at high temperature under argon atmosphere (500 °C, 2 h). The GO was partially reduced to G. The C elements on GO transform the amorphous $Cu_2(OH)_2CO_3$ and Cu_2O into crystalline Cu at high temperature. Finally, columnar, flower-like, bubble-like and teardrop-shaped Cu/GO nanocomposites were prepared. The layered structure of GO inhibits ion agglomeration, while GO contains a large number of electronegative groups (carboxyl and hydroxyl groups) that interact electrostatically with ions to load Cu nanoparticles onto GO.

3.1 The structures analysis of the Cu/GO nanocomposites

The structures of Cu/GO nanocomposites prepared with methanol, deionized water, ethanol and ethylene glycol as solvents were determined by X-ray diffraction (XRD), and the XRD patterns are shown in Fig. 2. The diffraction peaks at 2θ = 43.32°, 50.45° and 74.12° correspond to the (1,1,1), (2,0,0), (2,2,0) crystal surfaces of Cu. The relative intensity and positions of diffraction peaks are consistent with the standard card (PDF #85-1326). However, the diffraction peaks of Cu/GO which prepared in CH_3OH have a slight deviation to the right. That probably because the oxidation of sample, O have smaller atomic radius compared to Cu, when oxidation happen, smaller oxygen atoms replaced copper atoms, caused the lattice contraction. No other impurity peaks appear, which indicated that Cu/GO nanocomposites are high crystallinity.

In order to further characterize the elemental composition and oxidation state information of the Cu/GO nanocomposites, the valence electron states and bonding modes of GO and the teardrop-shaped Cu/GO nanocomposites prepared with ethylene glycol were characterized by XPS. XPS full spectra of GO and the teardrop-shaped GO/Cu nanocomposites (a), high-

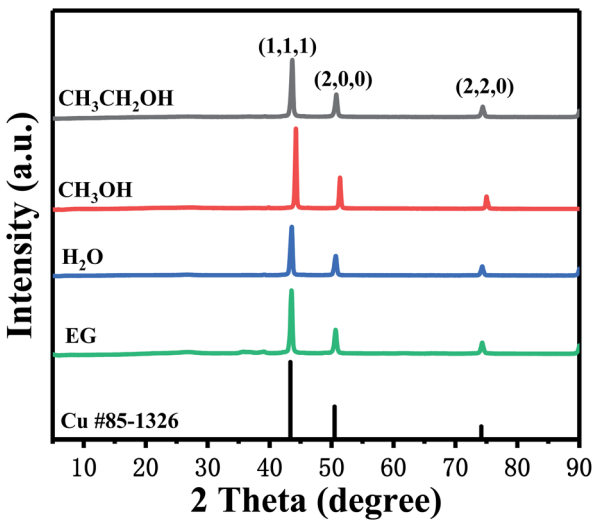

Fig. 2 XRD diffraction images of different morphology Cu/GO nanocomposites.

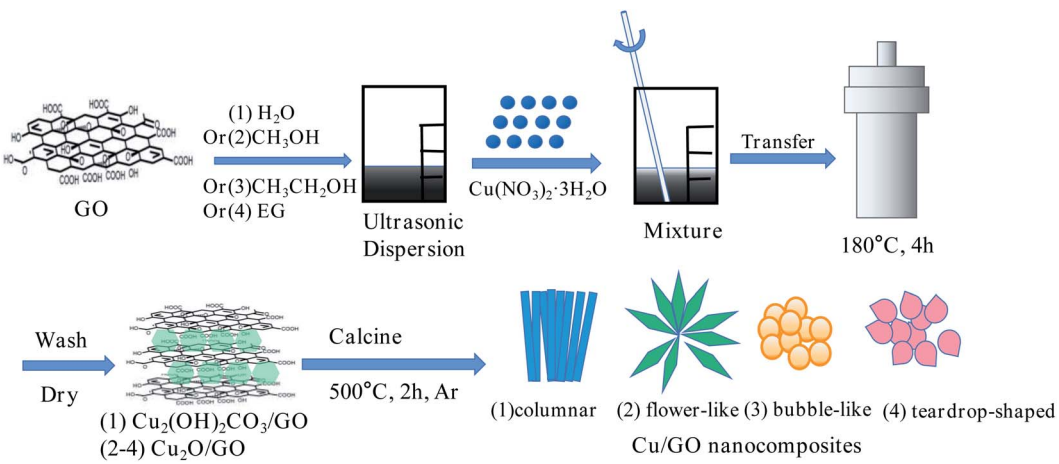

Fig. 1 Illustration of the preparation of different morphology Cu/GO nanocomposites.

resolution Cu 2p XPS spectra of the teardrop-shaped GO/Cu nanocomposites (b), high-resolution C 1s XPS spectra of GO (c) and the teardrop-shaped GO/Cu nanocomposites (d) were shown in Fig. 3. As can be seen from Fig. 3(a), the characteristic peaks of C 1s and O 1s appear of both GO and Cu/GO nanocomposites in the full spectrum. However, the relative strength of the O 1s in the Cu/GO nanocomposites is relatively weak. This is caused by the elimination of part GO oxygen groups during calcination at high temperature. We observed that two intense peaks at 933.1 eV and 952.5 eV correspond to the Cu $2p_{3/2}$ and Cu $2p_{1/2}$, and two accompanying peaks with binding energy of 943.1 eV and 962.9 eV in the high-resolution Cu 2p XPS spectrum of the GO/Cu nanocomposites in Fig. 3(b), which shows that the amorphous copper oxide changes into the copper with high crystallinity after high calcination. Meanwhile, three binding energy peak C–C/C=C (284.6 eV), C–OH/C–O–C (286.5 eV) and C=O (287.8 eV)[30] all appear in the high-resolution C 1s XPS spectra of GO and the teardrop-shaped GO/Cu nanocomposites in Fig. 3(c) and (d). But the relative strength of the C–OH/C–O–C in the GO/Cu nanocomposites is significantly lower than the peak strength in the GO. It further shows that most oxygen groups of GO were eliminated during high temperature calcination. In order to further characterize the valence state of Cu, the Auger electron spectrum was characterized, the result was shown in Fig. 3(e). Only one characteristic peak can be seen at 567.8 eV, which correspond to Cu.

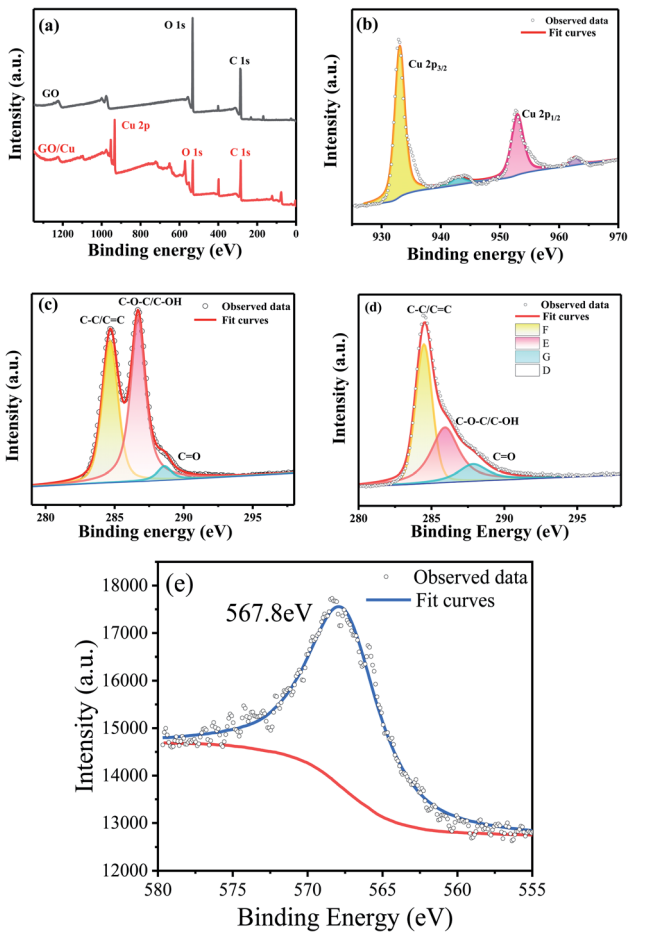

Fig. 3 XPS full spectra of GO and the teardrop-shaped Cu/GO nanocomposites (a), high-resolution Cu 2p XPS spectra of the teardrop-shaped GO/Cu nanocomposites (b), high-resolution C 1s XPS spectra of GO (c) and the teardrop-shaped GO/Cu nanocomposites (d), Auger spectra of teardrop-shaped Cu/GO nanocomposites (e).

The micromorphology of Cu/GO nanocomposites is crucial for the catalytic effect of the thermal decomposition of AP. Fig. 4 shows SEM images of Cu/GO nanocomposites prepared by methanol (a), deionized water (b), ethanol (c) and ethylene glycol (d) as solvents, STEM-EDX (e), HR-TEM micrograph (f) and EDX image (g) of the teardrop-shaped GO/Cu nanocomposites. As can be seen from Fig. 4(a–d), with the increase of solvent viscosity (methanol ~0.6 mPa s^{-1}, deionized water ~0.7972 mPa s^{-1}, ethanol ~0.983 mPa s^{-1}, ethylene glycol ~16.1 mPa s^{-1}), the growth rate of the catalyst crystals was gradually decreased,[31,32] the formation process is shown in Fig. 5. At high growth rates, the nanocrystals grow along both [0 0 1] and [0 1 0] directions,[33,34] forming regular lamellar structures, and with increasing reaction time, the lamellar crystals form flower-like structures through self-assembly, as shown in Fig. 4(a). With the increase of viscosity, the growth of the nanocrystals along the [0 0 1] direction was significantly hindered, mainly along the [0 1 0] direction, and eventually formed a columnar structure, as shown in Fig. 4(b). With further increase of viscosity, the growth rate decreases in both directions and smaller lamellar crystals are formed, and regular self-assembly cannot be performed, and nanoparticles of similar size are randomly stacked together to form a bubble-like structure, as shown in Fig. 4(c). When the viscosity of the solvent increases to a certain extent, the movement of the nanoparticles during assembly is hindered, and in contrast to (c), a tightly arranged teardrop-like structure is formed as shown in Fig. 4(d). The microstructure of the Cu/GO nanocomposites, especially the uniform dispersion of the Cu nanoparticles in the GO sheet, has important implications for the catalytic effect of AP thermal decomposition. We used scanning transmission electron microscopy-energy dispersion X-ray spectroscopy (STEM-EDX) tests to detect the element distribution of the teardrop-shaped GO/Cu nanocomposites. As can be seen from Fig. 4(e), the Cu elements are uniformly dispersed on the GO nanosheets, and no agglomeration phenomenon is observed. This is due to the fact that the GO surface contains a lot of oxygen-containing functional groups such as hydroxyl and carboxyl groups. Those groups provide more attachment sites for nanoparticles, effectively inhibiting the agglomeration of nanoparticles and uniformly dispersing Cu/GO nanocomposites over the lamella of graphene. Due to the large number of oxygen-containing functional groups on the GO surface, the Cu/GO nanocomposites have a certain amount of oxygen. Besides, the oxygen-containing groups eliminated in the process of calcination, the free oxygen can adsorb with copper, result in oxygen gathered in where copper located. More importantly, the sampling depth of EDX is about 1 μm, after placed some time in air, the oxidation of the surface of copper also made the content of oxygen higher. That is also observed in XRD diffraction image of flower-like Cu/GO nanocomposites

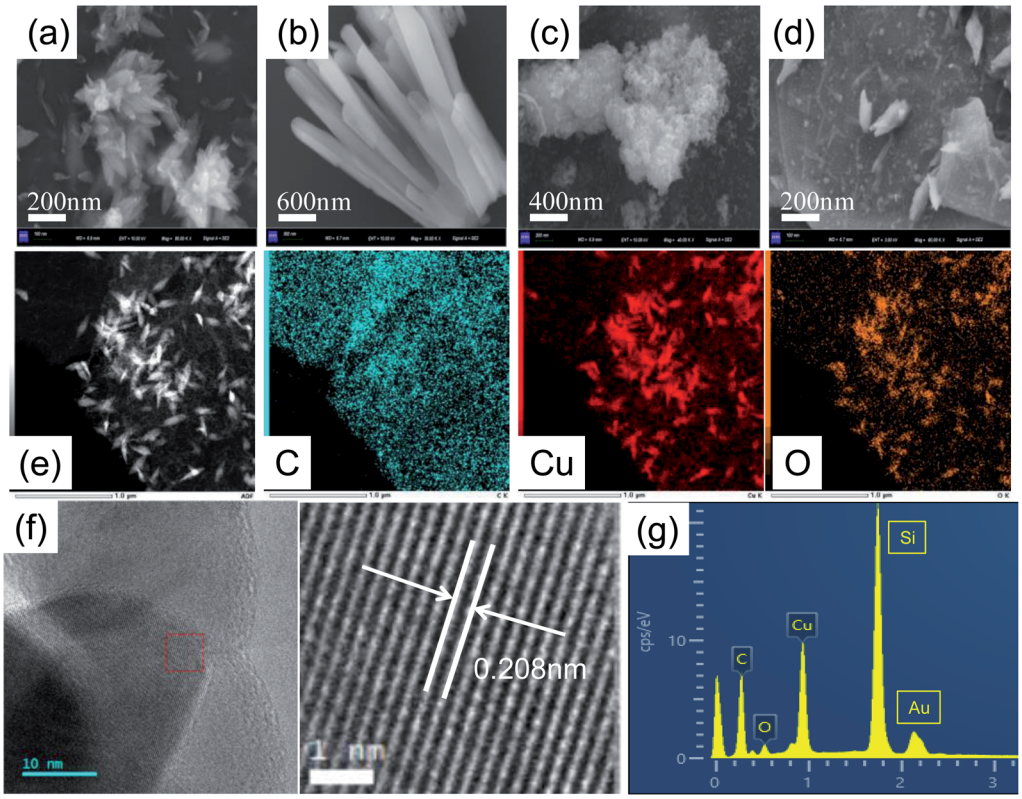

Fig. 4 SEM images of Cu/GO nanocomposites prepared by methanol (a), deionized water (b), ethanol (c) and ethylene glycol (d) as solvents, STEM-EDX (e), HR-TEM micrograph (f) and EDX image (g) of the teardrop-shaped GO/Cu nanocomposites.

(Fig. 2). The lattice stripe of Cu can be clearly observed from Fig. 4(f). The crystal surface spacing of the nanoparticles calculated by Nanoscope Analysis software is 0.208 nm, corresponding to the (1,1,1) crystal surface of Cu,[35] which is consistent with the results of XRD and XPS, indicated that Cu/GO nanocomposites was successfully prepared.

The morphology of nanoparticles has a significant effect on the specific surface area, and in general, the larger the specific surface area, the better the catalytic performance.[28] As a fuel speed catalyst for solid propellant, the large specific surface area of the Cu/GO nanocomposites expose more active sites, thus improving the catalytic activity. Therefore, the specific surface area and porous structure characteristics of different morphology Cu/GO nanocomposites were studied by N_2 adsorption–desorption isotherm method. The N_2 adsorption detachment curvature and aperture distribution curves are shown in Fig. 6. As can be seen from Fig. 6, the nitrogen adsorption–desorption curve of the Cu/GO nanocomposites presented the H3 characteristic hysteresis ring-type IV isotherm. The pore size distribution ranges from 2 to 50 nm, indicating that it has layered mesopore structure characteristics and more small aperture sizes. As shown in Table 1, the specific surface area of Cu/GO was calculated by BET method. All four Cu/GO nanocomposites have large surface area. And the specific surface area of teardrop-shaped Cu/GO

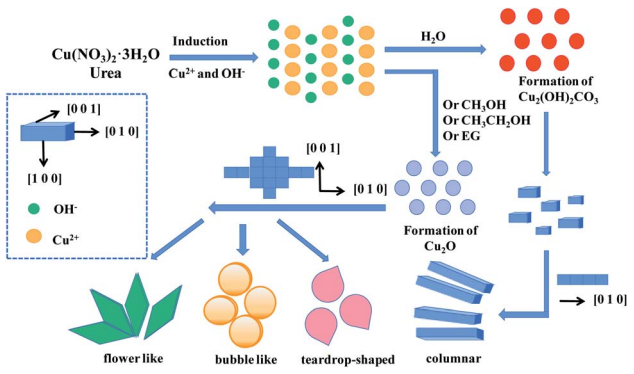

Fig. 5 Diagram of the formation process of the Cu/GO nanocomposites.

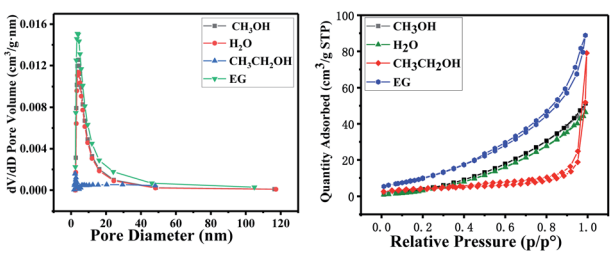

Fig. 6 N_2 adsorption/desorption isotherms and pore size distribution of Cu/GO nanocomposites with different morphologies.

Table 1 Specific surface area of Cu/GO nanocomposites with different morphologies

Samples	Specific surface area/m^2 g^{-1}
Bubble-like	13.28
Columnar	19.30
Flower-like	22.48
Teardrop-shaped	39.77

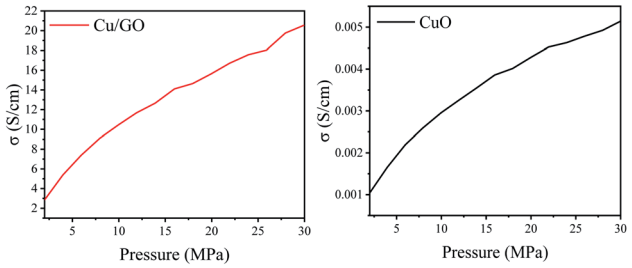

Fig. 7 The conductivity of teardrop-shaped Cu/GO nanocomposites and commercial copper oxide.

nanocomposites prepared with ethylene glycol as solvent can reach 39.77 m^2 g^{-1}.

The conductivity of catalyst is important in electron transfer. Higher conductivity means higher catalytic activity. The conductivity of teardrop-shaped Cu/GO nanocomposites and commercial copper oxide were characterized. As shown in Fig. 7, the conductivity of Cu/GO nanocomposites is much better than commercial CuO (150–250 nm), which is widely used as catalyst. With high conductivity, Cu/GO nanocomposites can accelerate the rate of electron transfer and speed of O_2 to O_2^- conversion.

3.2 The catalytic performance of the Cu/GO nanocomposites for thermal decomposition of AP

3.2.1 The catalytic performance analysis of the Cu/GO nanocomposites for thermal decomposition of AP. The effects of different morphology Cu/GO nanocomposites catalytic performance for thermal decomposition of AP were investigated by the TG-DSC method. Fig. 8 shows TG curves (a), DTG curves (b), DSC curves (c) and exothermic histograms (d) of 5 wt% the Cu/GO nanocomposites and AP blends. The TG curves, DTG curves and DSC curves of the Cu/GO nanocomposites that placed a month were shown in Fig. S2.† It can be seen from Fig. 8(a and b) that pure AP has two thermal weight loss intervals, corresponding to two intervals of 290–340 °C and 340–410 °C (low temperature decomposition stage and high temperature decomposition stage), and add 5 wt% of Cu/GO nanocomposites with different morphologies, the maximum decomposition rate temperature of AP and Cu/GO nanocomposites blends all gradually shifted to low temperature. Fig. 8(c) shows that pure AP exhibits an endothermic peak at 244.3 °C, corresponding to the oblique squared crystal pattern transition of AP to a cubic crystal pattern,[36,37] and two exothermic peaks appear at 303.8 °C and 426.3 °C, which are the low temperature and high temperature decomposition stages of AP.[38,39] When 5 wt% of the different morphology Cu/GO nanocomposites was added, both low temperature and high temperature decomposition peaks move gradually towards the low temperature direction, but had no effect on the crystal transformation process of AP. Therefore, Cu/GO nanocomposites with different morphologies have significant catalytic effects on the thermal decomposition of AP. When 5 wt% of the columnar, flower, bubble-like and teardrop-shaped Cu/GO nanocomposites were added, the corresponding high temperature decomposition temperature of AP decreased by 82.6 °C, 72.6 °C, 76.7 °C, and 80.8 °C, the exothermic heat released increased by 2685.6 J g^{-1}, 2574.8 J g^{-1}, 3280.4 J g^{-1} and 3749.0 J g^{-1}, respectively. Among them, the comprehensive catalytic effect of teardrop-shaped Cu/GO nanocomposites is the best, and the total heat release is increased to the original ten times.

It is interesting that four morphology Cu/GO nanocomposites were placed in the air after 1 month, the total heat release of Cu/GO/AP is not reduced. As shown in Fig. 8(d), four morphologies of Cu/GO nanocomposites still have good catalytic effect on AP. This is attributed to the strong catalytic activity of pure metal nanoparticles, GO accelerated electron movement of lamellar structure, and GO inhibition of nanoparticle agglomeration while also inhibiting the multiple effects of nanoparticles in oxidation in air.

The comparison of the decomposition temperature and the heat release of different catalysts on AP thermal decomposition was shown in Table 2. It can be seen that, four Cu/GO nanocomposites with different morphologies have similar decomposition temperature with different types of CuO, PbO, $CuFe_2O_4$, $[Cu(vimi)_4]DCA_2$. More importantly, the heat release of four Cu/GO nanocomposites with different morphologies is much higher than other normal catalysts.

3.2.2. The catalytic kinetic analysis of the Cu/GO nanocomposites for thermal decomposition of AP. In order to

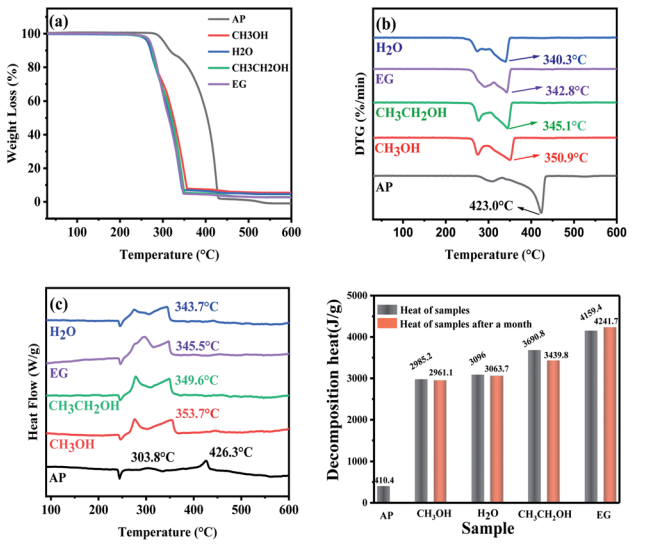

Fig. 8 TG curves (a), DTG curves (b), DSC curves (c) and exothermic histograms (d) of 5 wt% the Cu/GO nanocomposites and AP blends.

Table 2 Comparison of the decomposition temperature and the heat release of different catalysts on AP thermal decomposition

Sample	Decomposition temperature (°C)	Heat release (J g^{-1})	Ref.
Flower-like Cu/GO	353.7	2985.2	This work
Columnar Cu/GO	343.7	3096	This work
Bubble-like Cu/GO	349.6	3690.8	This work
Teardrop-shaped Cu/GO	345.5	4159.4	This work
CuO	353.8	1028	28
Flower-like CuO	353.17	1211	40
CuO/GO	337	1543.5	41
Nano PbO	400.9	1587	8
Hollow flower-like nickel particles (40 nm)	332	1163	10
Hollow flower-like nickel particles (200 nm)	374	697.2	10
[Cu(vimi)$_4$] DCA$_2$ (3%)	327	1599.2	12
$CuFe_2O_4$/g-C_3N_4 (2.5%)	318.6	1602	13
$CuFe_2O_4$/GO	331.4	1450	13
$CuFe_2O_4$	331.8	1115	13

further investigate the catalytic performance for thermal decomposition of AP by different morphology Cu/GO nanocomposites, four nanocomposites were mixed with AP (mass ratio is 5 : 95), and performed TG-DSC test at different heating rates (5 K min^{-1}, 10 K min^{-1}, 15 K min^{-1}, 20 K min^{-1}). According to the relationship between the peak exothermic heat and the heating rate, the kinetic parameters (activation energy and the leading factor) of AP under Cu/GO nanocomposites catalysis can be obtained. The relationship between thermal decomposition and heating rate of AP can be described by Kissinger's equation:

$$\ln(\beta + T_p^2) = \ln(AR/E_a) - E_a/RT_p$$

In this equation, β is the heating rate, T_p is the peak temperature of the AP high-temperature decomposition peak, E_a is the activation energy, R is the ideal gas constant, and A is the leading factor. As can be seen from the Kissinger equation, $\ln(\beta/T_p^2)$ and $(1/T_p)$ are linear relations. The line is fitted with $\ln(\beta/T_p^2)$ as the ordinate and $(1/T_p)$ as the abscissa. The activation energy and leading factor of AP thermal decomposition can be obtained from the slope and intercept of the straight line.

Fig. S3† shows the TG curves, DTG curves, and DSC curves of pure AP and AP in the presence of different morphology Cu/GO nanocomposites. Taking the thermal decomposition curve of AP as an example, as the heating rate increases, the TG, DTG and DSC curves move to the high temperature direction. This is due to the rapid heating rate of the temperature lead to the increase of gradient inside the system, which made the inhomogeneous heating of AP, caused the decomposition of AP at a higher temperature. Through the Kissinger equation, the liner fitting results of pure AP and AP in the presence of different morphology of Cu/GO were fitted. The fitting results were shown in Fig. 9. The corresponding kinetic parameters was shown in Table 3. The results showed that all four nanocomposites can reduce the activation energy of AP thermal decomposition, indicating that the existence of composites make the decomposition of AP proceed at lower temperature. In addition, the catalytic activities of Cu/GO nanocomposites with different morphologies in this work were compared with different catalysts. The Table 4 showed the comparison of the activation energy E_a of AP thermal decomposition with different catalysts given in recent literature. According to those results, Cu/GO nanocomposites have excellent catalytic action and most heat release. Among four Cu/GO nanocomposites, the teardrop-shaped Cu/GO nanocomposites is the most desirable catalyst.

3.2.3 The catalytic mechanism analysis of the Cu/GO nanocomposites for thermal decomposition of AP. In order to further investigate the catalytic mechanism of AP thermal decomposition by Cu/GO nanocomposites, Cu/GO-AP mixtures were analyzed by TG-IR. Fig. 10 shows the Three-dimension thermogravimetry-FTIR spectrum of the gas phase in the thermal degradation of teardrop-shaped Cu/GO-AP mixtures and FTIR spectrum at different temperature. When AP was mixed with Cu/GO nanocomposites, the main gas product is NH_3 (3400–3800 cm^{-1}), N_2O (2142–2267 cm^{-1}, 1237–1356 cm^{-1}), HCl (2679–3086 cm^{-1}) and NO_2 (1523–1678 cm^{-1}). In addition to the characteristic peaks of the AP decomposition products, the characteristic peaks of CO_2 (2270–2400 cm^{-1}, 610–730 cm^{-1}) also appeared. It shows that the oxidation

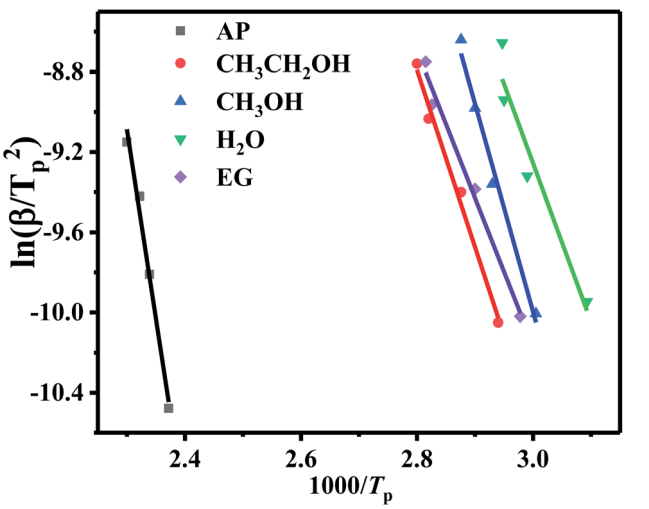

Fig. 9 Linear relationship between $\ln(\beta/T_p^2)$ and $(1000/T_p)$ of pure AP and AP with different morphology Cu/GO nanocomposites (the scatter plot is the experimental data and the straight line is the linear fit result).

Table 3 Table of kinetic parameters

Sample	E_a (kJ mol^{-1})	A (min^{-1})	r
AP	156.89	1.5×10^{16}	0.994
Bubble-like Cu/GO-AP mixtures	73.41	7.4×10^{7}	0.995
Flower-like Cu/GO-AP mixtures	86.22	1.5×10^{10}	0.992
Columnar Cu/GO-AP mixtures	65.7	1.1×10^{7}	0.967
Teardrop-shaped Cu/GO-AP mixtures	61.19	1.1×10^{6}	0.994

Table 4 Comparison of the activation energy E_a of AP thermal decomposition with different catalysts

	E_a (kJ mol^{-1})		
Catalyst	Pure AP	AP + catalyst	Ref.
Bubble-like Cu/GO	156.89	73.41	This work
Flower-like Cu/GO	156.89	86.22	This work
Columnar Cu/GO	156.89	65.7	This work
Teardrop-shaped Cu/GO	156.89	61.19	This work
CuO	213.4	86.7	42
Linear nano-MnO_2	203.87	195	43
Sea-urchin nano-MnO_2	203.87	150	43
G/CuO	129	71.47	44
Al/G/CuO	129	56.18	44
2% N–CuO/PbO	156.7	102.3	8
0.5% $CuFe_2O_4$/g-C_3N_4	161	116.4	13

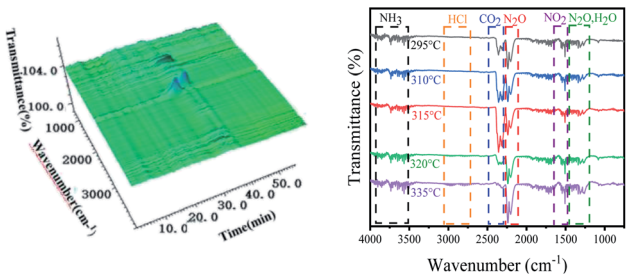

Fig. 10 Three-dimensional thermogravimetry–FTIR spectrum of the gas phase in the thermal degradation of teardrop-shaped Cu/GO-AP mixtures and gas analysis for Cu/GO-AP mixtures at different temperature.

products produced in the process of AP decomposition reacted with GO, and produced CO_2. As GO burned continuously, the NO_2 and N_2O content was increasing, indicating that the decomposition of AP is more intense.

The catalytic process of Cu/GO-AP mixtures is shown in Fig. 11. In the low temperature decomposition stage, AP partially decomposes to produce NH_3 and $HClO_4$. Then REDOX reaction occurs in the gas phase, releasing a small amount of heat. In the high temperature decomposition stage, AP is completely decomposed, which is the main decomposition process of AP thermal decomposition. In this stage, a large quantity of heat was released.

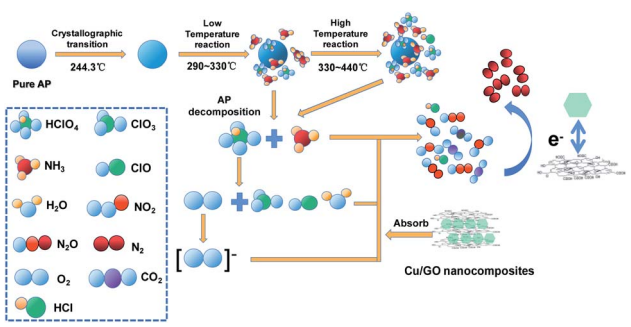

Fig. 11 Schematic diagram of thermal decomposition the Cu/GO/AP nanocomposites.

$$NH_4^+ + ClO_4^- = NH_3(a) + HClO_4(a) = NH_3(g) + HClO_4(g)$$

The main process of AP decomposition is caused by the REDOX reaction of decomposition products of $HClO_4$ with NH_3 in the gas phase. If the gas molecule diffuses and escapes, then the decomposition product of $HClO_4$ cannot fully react with NH_3. Cu/GO nanocomposites as carriers for AP thermal decomposition reactions have large specific surface area, which gives the ability to adsorb gaseous molecules. The folds of the GO surface can also adsorb large amounts of gas molecules, providing a large number of active sites. Thus, in the second exothermic decomposition step of AP, Cu/GO nanocomposites adsorb gas-reactive molecules on their surface to react on the condensed phase. Meanwhile, there are many defects on the Cu nanoparticle lattice, and nitrogen oxides can easily react with Cu to form copper oxide.[45,46] AP decomposition is accelerated by catalyzing the decomposition of nitrogen oxides.

$$Cu + N_2O = CuO + N_2$$

$$4Cu + 2NO_2 = 4CuO + N_2$$

Moreover, due to the high thermal conductivity and high electrical conductivity, the rate of electron transfer and speed of O_2 to O_2^- conversion accelerated. Finally, the AP decomposition heat increased, and the thermal decomposition rate increased.[14]

4. Conclusions

In summary, four novel morphologies (columnar, flower-like, bubble-like and teardrop-shaped) Cu/GO nanocomposites were prepared and characterized. It was confirmed that the four morphological Cu/GO nanocomposites have large specific surface area and excellent catalytic performance for thermal decomposition of AP. Among them, the teardrop-shaped Cu/GO nanocomposites has the largest specific surface area (39.77 m^2 g^{-1}) and the best catalytic performance. When 5 wt% of the Cu/GO nanocomposites was added, the decomposition temperature of AP decreased from 426.3 °C to 345.5 °C, the exothermic heat released from the decomposition of AP increased from 410.4 J g^{-1} to 4159.4 J g^{-1}. Through the studies on pyrolysis volatiles of the Cu/GO-AP mixtures, it can be concluded that the catalytic mechanism of the Cu/GO nanocomposites for thermal decomposition of AP. Moreover, due to the presence of the layered structure GO, both the agglomeration of Cu nanoparticles and the oxidation of Cu nanoparticles in air are inhibited. All the results indicated that the Cu/GO nanocomposites had great potential applications in the future.

Conflicts of interest

There are no conflicts to declare.

Acknowledgements

This work was financially supported by the Special Planning Projects (70902010115).

Notes and references

1 P. Ren, H. Wang, G. Zhou, J. Li, Q. Cai, J. Yu and Y. Yuan, *Chin. J. Aeronaut.*, 2021, **34**, 208–224.
2 S. Jain, S. Chakraborty and L. Qiao, *Combust. Flame*, 2019, **206**, 282–291.
3 I. P. S. Kapoor, P. Srivastava and G. Singh, *Propellants, Explos., Pyrotech.*, 2009, **34**, 351–356.
4 J. Wang, W. Zhang, Z. Zheng, Y. Gao, K. Ma, J. Ye and Y. Yang, *J. Alloys Compd.*, 2017, **724**, 720–727.
5 J. M. Gao, L. Wang, H. J. Yu, A. G. Xiao and W. B. Ding, *Propellants, Explos., Pyrotech.*, 2011, **36**, 404–409.
6 J. N. Modanlou and A. Eslami, *J. Therm. Anal. Calorim.*, 2019, **136**, 913–923.
7 G. Marothiya, C. Vijay, K. Ishitha and P. A. Ramakrishna, *Combust. Flame*, 2017, **182**, 114–121.
8 G. Zhang, B. Gou, Y. Yang, M. Liu, X. Li, L. Xiao, G. Hao, F. Zhao and W. Jiang, *ACS Omega*, 2020, **5**, 32667–32676.
9 X. Zhou, C. Hu, X. Liu, W. Chen, Q. Tang and Y. Li, *J. Rare Earths*, 2020, **38**, 108–112.
10 T. Zhang, H. Shi, Y. Zhang, Q. Liu, W. Fei and T. Wang, *Appl. Surf. Sci.*, 2021, **552**, 149506.
11 D. N. Ma, X. M. Li, X. Q. Wang and Y. J. Luo, *Eur. J. Inorg. Chem.*, 2021, **10**, 982–988.
12 G. Lei, Y. zhong, Y. xu, F. yang, J. Bai, Z. Li, J. Zhang and T. Zhang, *Chin. J. Chem.*, 2021, **39**, 1193–1198.
13 C. Wan, J. Li, S. Chen, W. Wang and K. Xu, *J. Anal. Appl. Pyrolysis*, 2021, **160**, 105372.
14 S. Wang, B. Ye, C. An, J. Wang and Q. Li, *J. Mater. Sci.*, 2019, **54**, 4928–4941.
15 L. Liu, F. Li, L. Tan, L. Ming and Y. Yi, *Propellants, Explos., Pyrotech.*, 2004, **29**, 34–38.
16 J. Wang, X. Lian, Q. Yan, D. Gao, F. Zhao and K. Xu, *ACS Appl. Mater. Interfaces*, 2020, **12**, 28496–28509.
17 C. Sang, S. Jin, G. Li and Y. Luo, *J. Sol-Gel Sci. Technol.*, 2021, **98**, 559–567.
18 S. H. Ba, S. Y. Cai, F. Lu and J. Chin, *Energy Mater.*, 2021, **29**, 460–470.
19 M. Nekoeinia, F. Salehriahi, O. Moradlou, H. Kazemi and S. Yousefinejad, *New J. Chem.*, 2018, **42**, 9209–9220.
20 S. Isert, L. Xin, J. Xie and S. F. Son, *Combust. Flame*, 2017, **183**, 322–329.
21 P. Chandrababu, J. Thankarajan, V. S. Nair and R. Raghavan, *Thermochim. Acta*, 2020, **691**, 178720.
22 S. Reshmi, K. B. Catherine and C. P. R. Nair, *Int. J. Nanotechnol.*, 2011, **8**, 979–987.
23 X. Cui, P. Ren, D. Deng, J. Deng and X. Bao, *Energy Environ. Sci.*, 2016, **9**, 123–129.
24 M. Li, L. Zhang, Q. Xu, J. Niu and Z. Xia, *J. Catal.*, 2014, **314**, 66–72.
25 M. Zhang, F. Zhao, Y. Yang, J. Zhang, N. Li and H. Gao, *CrystEngComm*, 2018, **20**, 7010–7019.
26 W. Wang, S. Guo, D. Zhang and Z. Yang, *J. Saudi Chem. Soc.*, 2019, **23**, 133–140.
27 W. Wang, B. Liu, K. Xu, Y. Zu, J. Song and F. Zhao, *Ceram. Int.*, 2018, **44**, 19016–19020.
28 Y. Hu, S. Yang, B. Tao, X. Liu, K. Lin, Y. Yang, R. Fan, D. Xia and D. Hao, *Vacuum*, 2019, **159**, 105–111.
29 L. Chen, L. Li and G. Li, *J. Alloys Compd.*, 2008, **464**, 532–536.
30 J. Zhi, Z. Feng-Qi and J. Propul, *Technol*, 2002, **23**, 258–261.
31 S. Chaturvedi and P. N. Dave, *J. Saudi Chem. Soc.*, 2013, **17**, 135–149.
32 Y. Yuan, W. Jiang, Y. Wang, P. Shen, F. Li, P. Li, F. Zhao and H. Gao, *Appl. Surf. Sci.*, 2014, **303**, 354–359.
33 M. A. Dar, Q. Ahsanulhaq, Y. S. Kim, J. M. Sohn, W. B. Kim and H. S. Shin, *Appl. Surf. Sci.*, 2009, **255**, 6279–6284.
34 Q. Zhang, K. Zhang, D. Xu, G. Yang, H. Huang, F. Nie, C. Liu and S. Yang, *Prog. Mater. Sci.*, 2014, **60**, 208–337.
35 Y. Xie, B. Liu, Y. Li, Z. Chen, Y. Cao and D. Jia, *New J. Chem.*, 2019, **43**, 12118–12125.
36 K. Kishore and K. Sridhara, *Solid propellant chemistry: condensed phase behaviour of ammonium perchlorate-based solid propellants*, Defence Research & Development Organisation, Ministry of Defence, 1999.
37 F. Solymosi and K. Fanagy, *Symp. (Int.) Combust., [Proc.]*, 1967, **11**, 429–437.
38 W. A. Rosser and S. H. Inami, *Combust. Flame*, 1968, **12**, 427.
39 P. W. M. Jacobsete, *Combust. Flame*, 1969, **13**, 419.
40 Y. Xu, D. Chen, X. Jiao and K. Xue, *Mater. Res. Bull.*, 2007, **42**, 1723–1731.
41 H. Akbi, S. Rafai, A. Mekki, S. Touidjine, M. A. Fertassi and D. E. Kadri, *J. Organomet. Chem.*, 2022, **957**, 122159.
42 Y. Zhang, K. Li, J. Liao, X. Wei and L. Zhang, *Appl. Surf. Sci.*, 2020, **499**, 143875.
43 Y. Chen, K. Ma, J. Wang, Y. Gao, X. Zhu and W. Zhang, *Mater. Res. Bull.*, 2018, **101**, 56–60.
44 M. A. Fertassi, K. T. Alali, Q. Liu, R. Li, P. Liu, J. Liu, L. Liu and J. Wang, *RSC Adv.*, 2016, **6**, 74155–74161.
45 W. Sun, X. Ling, W. Wei, H. Hu, Z. Jiang, Z. Yan and J. Xie, *Appl. Surf. Sci.*, 2019, **493**, 710–718.
46 A. T. Aqueel Ahmed, B. Hou, H. S. Chavan, Y. Jo, S. Cho, J. Kim, S. M. Pawar, S. N. Cha, A. I. Inamdar, H. Kim and H. Im, *Small*, 2018, **14**, 1800742.